Direct Mapping of Ionic Transport in a Si Anode on the Nanoscale: Time Domain Electrochemical Strain Spectroscopy Study

Stephen Jesse,[†] Nina Balke,[†] Eugene Eliseev,[‡] Alexander Tselev,[†] Nancy J. Dudney,[†] Anna N. Morozovska,[‡] and Sergei V. Kalinin[†,*]

[†]Oak Ridge National Laboratory, Oak Ridge, Tennessee 37831, United States, and [‡]National Academy of Science of Ukraine, Kiev, Ukraine

ABSTRACT

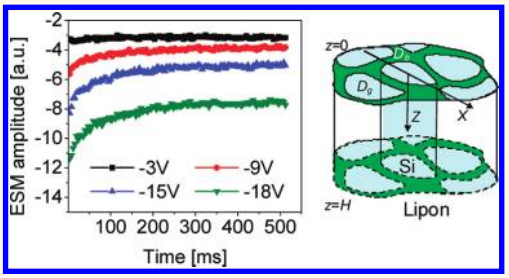

Local Li-ion transport in amorphous silicon is studied on the nanometer scale using time domain electrochemical strain microscopy (ESM). A strong variability of ionic transport controlled by the anode surface morphology is observed. The observed relaxing and nonrelaxing response components are discussed in terms of local and global ionic transport mechanisms, thus establishing the signal formation mechanisms in ESM. This behavior is further correlated with local conductivity measurements. The implications of these studies for Si-anode batteries are discussed. The universal presence of concentration–strain coupling suggests that ESM and associated time and voltage spectroscopies can be applied to a broad range of electrochemical systems ranging from batteries to fuel cells.

KEYWORDS: time domain electrochemical strain microscopy · Si anode · lithium ion

Transport of charged species in solids directly underpins the functionality of multiple information and energy materials and devices. These include cation, oxygen vacancy, and proton transport in energy storage[1] and conversion systems,[2,3] as well as in memristive and electroresistive materials.[4,5] Design and optimization of cathode and anode materials and architectures necessitates understanding phenomena such as interface-enabled diffusion,[6,7] inhomogeneous distribution of mobile species,[8] and the role of microstructure on diffusion and migration transport on the nanometer scale.

This problem is particularly of interest in the context of developing high energy density anode materials with long life times. Materials such as Si, Sn, and Ge with high Li-ion capacities tend to be highly susceptible to irreversible capacity loss, partially attributable to mechanical degradation and amorphization.[9,10] The mechanism of Si-anode operation was extensively studied using Mossbauer spectroscopy,[11] X-ray scattering,[12] and first principle theory.[13,14] The evolution of strains was studied using *in situ* topographic imaging of patterned anodes by Dahn,[15] establishing both functionality and conditions for mechanical stability. Furthermore, the universal relationship between strain development and capacity was developed.[16] It was realized that the irreversible capacity loss can be minimized if the mechanical degradation can be reduced, and strategies to mitigate this effect based on nanostructuring,[17] composite architectures,[18] and binder design[19] were suggested. However, despite multiple studies, the nanoscale picture of strain development in the Si anode and its relationship to local microstructure and degradation mechanisms is still incomplete. This understanding will greatly benefit from spatially resolved studies of local electrochemical and ionic processes within the anode or at the anode surfaces. These studies can potentially be used to correlate local electrochemical functionality with microstructure and establish mechanisms for capacity loss and fading, as well as to suggest strategies for materials optimization.

The classical electrochemical methods[20] for probing ionic transport rely on the use of appropriate transducer electrodes that link the electrochemical potential of ions in the

* Address correspondence to sergei2@ornl.gov.

Received for review August 16, 2011 and accepted November 4, 2011.

Published online November 04, 2011
10.1021/nn203141g

solid to the electrochemical potential of the electrons. However, large characteristic impedances limit this approach to relatively large (≫1 μm) electrodes. Recently, we have demonstrated electrochemical strain microscopy (ESM) as well as associated voltage and time spectroscopies[21−23] as an approach for mapping ion dynamics through the detection of dynamic strain response to an applied periodic electric bias. Here, we probe local ionic transport in Si anodes through the direct measurements of bias-induced relaxation in the time domain.[24] The image formation mechanism in ESM time spectroscopy is established using a combination of analytical theory and numerical COMSOL modeling. This approach is used to explore time-dependent phenomena in an amorphous Si anode incorporated into a functional battery structure and their evolution with charging.

Electrochemical Strain Spectroscopy. Traditional approaches for probing ionic transport in electrochemical systems are based on the detection of frequency-dependent electronic current induced by the application of voltage to the system through macroscopic or mesoscopic[25−27] electrodes. This approach is used in a broad spectrum of time, frequency, and voltage spectroscopies including potential and galvanostatic intermittent titration techniques (PITT and GITT),[20,28−31] time-relaxation methods, and electrochemical impedance spectroscopy (EIS).[32] Additional specificity can be achieved through the use of selective (reversible *vs* ion-blocking) electrodes. However, the detection of Faradaic currents limits the measurements to relatively large (>1 μm) systems as limited by the associated impedances.

An alternative to Faradaic current detection is to detect electrochemical strains induced by chemical (*e.g.*, dilatometry)[8] or electrical stimulus. In particular, the latter approach can be readily scaled to the nanometer level since electric fields can be concentrated to a small volume of material and dynamic strains can be measured at the ∼3−10 pm level. This approach is well-established for piezoelectric materials (piezoresponse force microscopy)[33,34] and has recently been extended to electrochemical systems giving rise to electrochemical strain microscopy and spectroscopy.[35]

To illustrate the detection limits of strain *versus* current detection, we note that the ∼pA currents correspond to ∼10^7 e^-/s flow. In the region of interest for electrochemical measurements, the total data accumulation time is commensurate with the diffusion times and is on the order of seconds for diffusion lengths in the ∼10 nm regime (and significantly larger for micrometer scales). This simple estimate suggests that Faradaic current detection is limited to ∼10^7 ions for ∼10 nm scale and rapidly increases for larger length scales. In comparison, the detection limits for strain detection can be estimated from the typical values of Vegard strain tensor defining chemical expansivity of a material. For typical material such as $Li_{1-x}CoO_2$, the lattice parameter change in x from 0 to 0.5 is ∼40 pm.[36] Given (experimentally determined) AFM sensitivity of 2−4 pm for dynamic detection, Li-state change by just 10% can be measured on the *single* unit cell level. Note that the detection limits of SPM in static and dynamic regimes are extensively discussed.[37−40] The lateral size of signal generation volume can be either estimated from Hertzian contact mechanics (∼3−5 nm) or established self-consistently from experimental observations (below 10 nm for Si studied here). This simple analysis suggests that 10^2−10^3 ions can be detected assuming that strong coupling between tip bias and ion concentration is established.

Application of a bias pulse to a localized (tip−surface contact radius is typically 3−20 nm) SPM tip in contact with a material surface (tip electrode ESM) or the electrochemical device structure (top electrode ESM) results in an electrochemical reaction in the tip−surface junction and redistribution of mobile ions by migration (field-driven) and diffusion (concentration-driven) mechanisms. For migration, the ionic flow is directly proportional to the electric field established in the materials. For diffusion, interfacial reactions at the tip−surface junction and internal interfaces driven by local electric fields generate an excess concentration of mobile ions that subsequently evolve according to the generalized Fick's law. If the system is biased, both transport mechanisms, migration and diffusion, operate simultaneously. As the electric field turned off, the condition of local electroneutrality leads to the classic ambipolar diffusion transport. In all cases, the local strains resulting from the changes in ion concentration will result in vertical and lateral surface displacements that can be detected by the SPM tip.

The natural limitation of direct measurements of the strain-bias curve (*i.e.*, local strain analog of charge−discharge measurements) by SPM is the significant times associated with ionic transport and relatively low sensitivity of SPM to slow (static) deformations as limited by 1/*f* noise. For example, the diffusion length of 3−30 nm (*i.e.*, comparable to typical tip−surface contact) corresponds to diffusion times of the order of ∼0.01−1 s (1−100 Hz) for diffusion coefficients of the order of 10^{-15} m^2/s. While feasible, these static measurements by SPM suffer from 1/*f* noise. Furthermore, multiple charge−discharge cycles may lead to rapid surface degradation common for electrochemical systems. Correspondingly, ESM measurements are performed in the differential detection mode when the slow (0.1−10 Hz) voltage sweep inducing electrochemical process is additionally modulated by a high-frequency (0.1−1 MHz) signal, and the periodic response amplitude and phase are detected as the ESM signal. Note that in a nonhysteretic system the use of a differential detection scheme measures the derivative

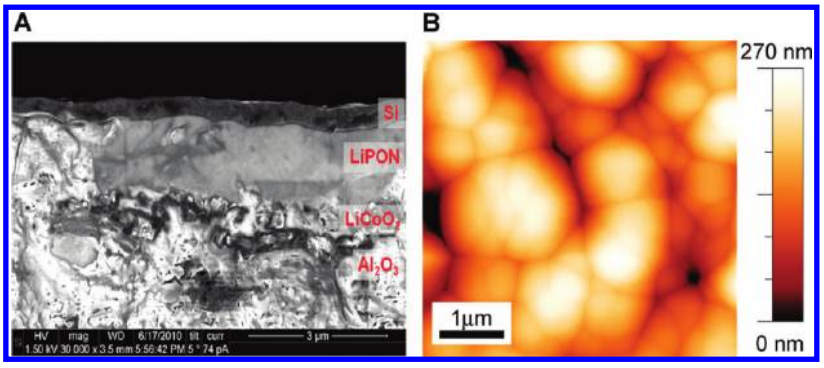

Figure 1. (A) SEM cross section image of the a-Si/LiPON/$LiCoO_2$ thin-film heterostructure. (B) Topography of the a-Si anode measured by AFM showing grain-like and grain-boundary-like features induced by the substrate.

of the response, providing the advantage of a significantly increased signal-to-noise ratio. For hysteretic systems, the relationship between the differential response and the signal is more complex but can be readily analyzed for known or postulated physical models.[35,41,42]

Time Domain ESM of a Si Anode. Here, we discuss the ESM approach for the direct measurement of the in-field (migration + diffusion) and off-field (diffusion) transport in solids using the differential detection mode combining a low-frequency pulse train with a superimposed high-frequency detection signal and elucidate the associated signal formation mechanisms. Specifically, we aim to establish whether the detected electrochemical strain is due to the local microstructure-related variability in diffusion fluxes or local electrochemical response at the tip−surface junction due to a local potential drop induced by finite conductivity of the Si anode. Subsequently, we aim to establish the evolution of the ESM signals with the state of the charge state of the anode.

As a model system, we have chosen an amorphous Si/LIPON/$LiCoO_2$ (film thicknesses of 320, 1070, and 530 nm, respectively) heterostructure[43] grown by radio frequency sputtering on Al_2O_3 substrates. A SEM image of the cross section of this thin-film battery is shown in Figure 1A. It has been found that the surface roughness of the Al_2O_3 substrate is transferred throughout the layered battery, resulting in topographic dips on the surface reminiscent of the grain boundaries in the amorphous Si anode, as shown in Figure 1B. In the following, we refer to these as boundary-like or grain-like features. Note that significant sharpness of the GB-like feature suggests that there are changes in material structure. However, given the lack of long-range crystalline order, these cannot be considered to be classical grain boundaries. Similar surface characteristics have been reported previously for a-Si layers on rough substrates (columnar growth).[44−47] Electrical bias was applied between the bottom current collector and the (nominally) grounded top anode, and the grounded conductive tip was used as a strain sensor. The preparation and structure of these devices is described in detail in refs 21 and 22. These structures offer a convenient model system that allows both high-resolution studies of Li-ion dynamics by SPM and tuning of the Si anode state through lithiation and cycling.

All measurements have been conducted on a Nanoman V (Bruker, Santa Barbara, CA) microscope equipped with a custom-developed Matlab/LabView data acquisition and control system. The top electrode and the tip (PPP-EFM, Nanosensors) are grounded, and the dc/ac bias has been applied through the current collector to the bottom electrode. The measurements are performed at room temperature in an ambient environment; that is, a water droplet is always present at the junction of the tip and the sample. Under these conditions, the water droplet can act as an electrolyte and irreversible extraction of Li through the top anode surface and subsequent reaction with ambient H_2O and CO_2 with formation of carbonates and hydroxides is possible. However, these processes are associated with irreversible changes of surface topography and formation of product particles. The latter can be detected by topographic imaging with nanometer resolution and are not observed in the present study (note that applications of high amplitude, >15−20 V, voltage pulses result in irreversible surface deformation due to nano-oxidation). The humidity effects on the Si nano-oxidation are well-recognized.[48] However, the latter will be observed as irreversible changes of surface topography. We further note that formation of a water droplet in the tip−surface junction can affect the distribution of ac and dc electric field in the tip−surface junction.[49,50] However, the experimentally measured sharpness of surface features in ESM maps suggests that there is no significant broadening of resultant potential distributions. Finally, ESM imaging and spectroscopy is complemented using classical conductive AFM probing electronic currents through tip−surface junction, previously extensively applied for electrochemical systems.[51−54]

The use of differential detection in dynamic SPM allows significant enhancement of the signal-to-noise ratio. Additionally, to amplify weak surface displacements using cantilever resonances,[41,55] ESM is

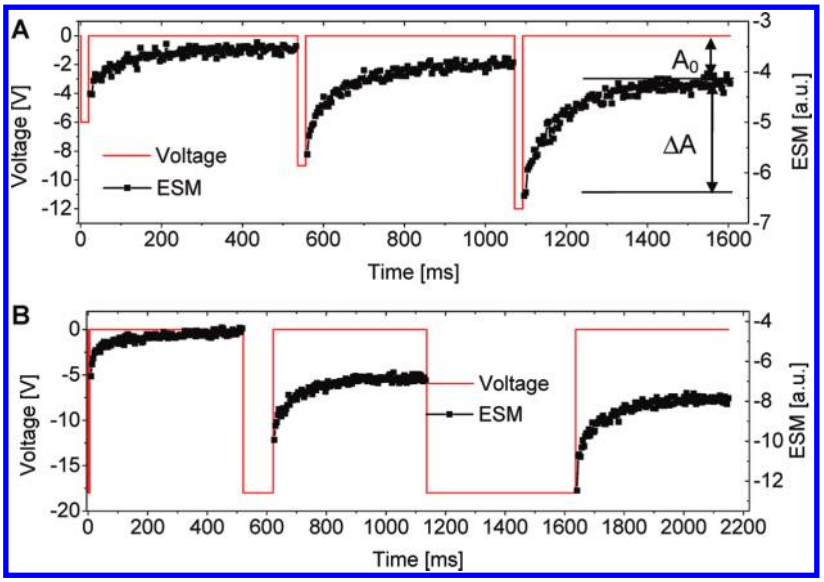

Figure 2. Experimentally observed time-dependent ESM signal after application of bias pulses of (A) varying amplitude and (B) lengths. Note the strong time dependence of local ESM signal reflecting relaxation of bias-induced Li-ion concentration disturbance. Strong relaxation is observed only at selected locations on the Si anode surface typically corresponding to grain-boundary-like features.

implemented in the band excitation (BE) mode,[56] in which the electrical excitation signal is digitally synthesized to have a uniform amplitude in a predefined frequency range. The range is chosen to be broad enough to contain the resonant frequencies of the cantilever at all locations on the sample surface. This approach allows the effects due to the variation of contact resonance frequency due to (topographically non-uniform) sample surfaces to be obviated and does not require (potentially unstable) frequency feedback.

Here, we use a BE bandwidth of 60 kHz centered at 430 kHz for a resonance peak width of 3−5 kHz. The variations of resonance frequency due to surface roughness and the large-scale changes due to grain structure and large-scale topographic gradients are on the order of 30 kHz. Note that the strong variability of the contact resonance frequency and lack of definitive relationship between the phase of driving voltage and response necessitates the use of band excitation (BE) or equivalent broad-band acquisition[57,58] or amplitude-based feedback methods[59] and obviates the use of standard phase-locked loop-based frequency tracking methods. The data analysis in BE and conversion of the measured 4D response *versus* time, frequency, and position data sets as applied for ferroelectric materials is discussed in detail elsewhere.[60,61]

Notably, at the high measurement frequencies (430 kHz compared to ∼1−100 Hz inverse Li diffusion times), the bias-induced Li mobility is likely to include both diffusion and migration contributions since the electric field may penetrate the semiconducting anode. We verify that the electromechanical response linearly depends on the amplitude V_{ac} of the BE signal up to driving voltages of ∼7 V_{ac} (Figure 3A). The linearity for small biases ensures the fidelity of the high-frequency (∼400 kHz) detection method employed here and suggests that it can be used as a measure of Li activity in the material.

To address the Li-ion transport kinetics directly, we perform differential strain measurements,[24] reminiscent of classical potentiostatic intermittent titration technique (PITT).[20] A short bias pulse of a predefined amplitude and duration is applied to the system, resulting in the redistribution of the mobile ions. Following the pulse, the ESM response is probed as a function of time at zero bias. Given the limitation of BE detection, the lower limit for detection times is ∼0.3 ms, whereas the top limit is defined by the stability of the system and can be as large as ∼100 s for single point measurements and ∼0.3−1 s for spatially resolved mapping (as limited by the total acquisition times for a 100 × 100 pixel image). Notably, this interval of probing times is ideally suited for probing ionic diffusion, with characteristic diffusion times for volumes typically probed by ESM on the order of 0.1−10 s. The typical relaxation of an electromechanical signal for different voltage amplitude and length is shown in Figure 2, providing the time dynamics of bias-induced ionic motion with a stationary tip placed at one of the boundary-like features. The increase in the ESM signal is a measure of the bias-induced Li-ion concentration change in the probed volume. It can be seen that the ESM signal relaxes to a constant value within 500 ms, whereas the constant value changes as a function of the voltage pulse amplitude. Phenomenologically, the relaxation curves can be described by the offset A_0, the relaxation amplitude ΔA, and the relaxation time τ, as illustrated in Figure 2A.

The effect of pulse duration for a constant pulse amplitude of −18 V and pulse amplitude for constant duration of 1 s on the measured time-dependent ESM response is shown in Figure 3B,C for a tip placed at one of the grain-boundary-like features. The longer pulse duration or higher pulse voltages result in a stronger Li redistribution as detected by high-frequency strain response. When the pulse length is fixed at 1 s and the pulse amplitude is varied (Figure 3C), a minimum of −4 V has to be applied in order to significantly change the Li concentration and thus induce the nonzero strain response of the battery, in agreement with previous voltage spectroscopy studies.[22] The dependence of the induced change in strain response on pulse length is approximately logarithmic in time and linear in pulse magnitude, as shown in Figure 3D. While we defer the detailed analysis to the future, it should be noted that similar behavior is observed for other SPM-based relaxation phenomena in disordered systems such as ferroelectric relaxors.[62−67]

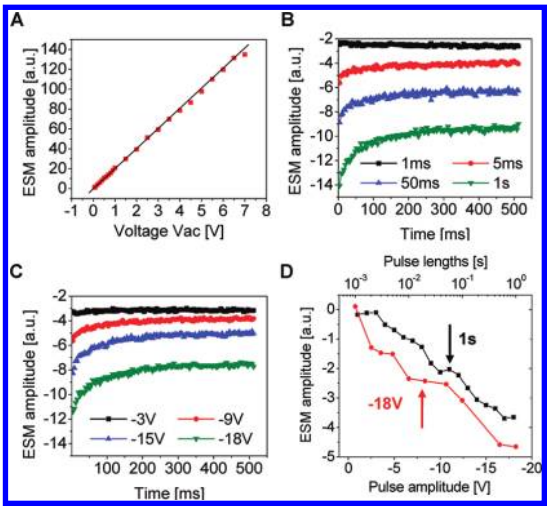

Figure 3. (A) Relationship between ESM amplitude and applied V_{ac} illustrating linearity of the response. (B) ESM amplitude relaxation as a function of pulse time for a constant pulse amplitude of −18 V. (C) Amplitude relaxation as a function of pulse magnitude for a constant pulse length of 1 s. (D) Dependence of relaxation amplitude as a function of pulse length and amplitude.

Qualitative Time Domain ESM Mapping. To determine spatial variability of transport behavior across the surface and correlate it with microstructure, ESM relaxation is measured at each spatial location over a dense square grid of 100 × 100 spatial locations. The resulting 4D data array is analyzed to extract the time dependence of the ESM signal at each spatial location.[60,61] The resulting 3D ESM time-coordinate array can be analyzed using direct functional fit[62,68] or multivariate statistical methods[68,69] to yield 2D spatial maps of position-dependent relaxation behavior, as discussed below. During the experiment, the sequence of two positive and two negative pulses is used, in order to (a) establish the reproducibility between first and second and third and fourth pulses (i = 1, 2, 3, 4) at a single location and (b) minimize the changes of the charge state of the electrochemical device inevitable under unipolar cycling. The probing bias sequence and the corresponding time-dependent ESM response for a grain interior and a grain-boundary-like location are shown in Figure 4A.

The data in Figure 4A illustrate the qualitative aspects of ESM relaxation dynamics on the Si-anode surface. Note that the offset (*i.e.*, static) ESM signal is almost zero in the center of grain-like features and shows clear anomalies at the grain-boundary-like features. This observation suggests that in the "grains" the bias-induced changes in Li concentration are reversible and the state of the sample is the same before and after the pulses. In this case, the relaxation amplitudes are low, as well. In the regions of high signal increase after

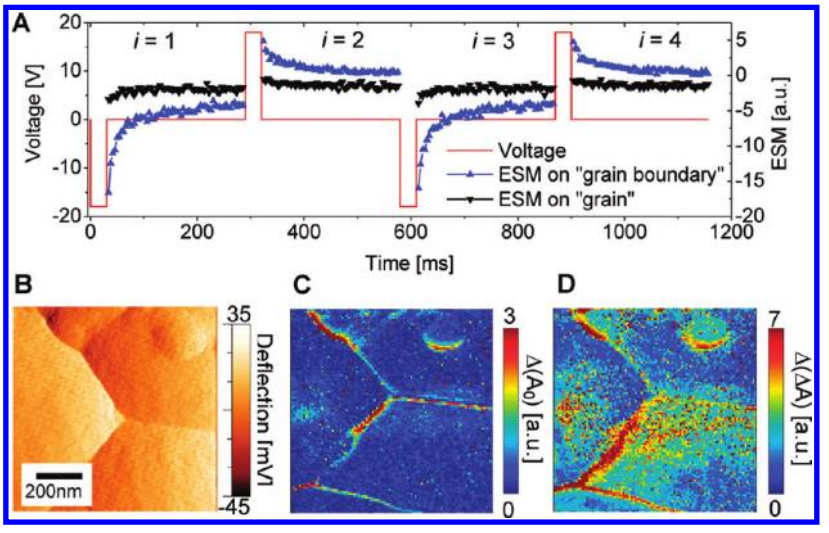

Figure 4. (A) Bipolar bias sequence and the corresponding time-dependent ESM response for a grain-like and grain-boundary-like location. (B) Surface deflection signal. (C) Map of difference in offset A_0. (D) Map of difference in relaxation amplitude ΔA between the first and second voltage pulse. Scan size is 1 μm.

the voltage pulses at the boundary-like features, the induced changes have a reversible (time-dependent) and irreversible (time-independent) contribution. Both depend on the polarity of the voltage pulse (compare $i = 1$ and $i = 2$ in Figure 4A). The negative voltage pulses applied to the bottom current collector induce a larger offset and relaxation amplitude than positive voltages. This is shown in Figure 4C,D, where the differences in offset and relaxation amplitude between the first and second voltage pulse are displayed for a spatially resolved measurement in the area shown in Figure 4B. The maps for first and third pulse, $i = 1, 3$, and second and fourth pulse, $i = 1, 4$, are virtually identical. This behavior can be expected since the overall number of measurement pulses is large ($\sim 2 \times 10^4$ per scan), and hence, cyclostationary behavior is established. Note that the ESM images show clear contrast varying on the $\sim$10 nm length scale, indicative of the high spatial resolution of the method.

Finally, we briefly address the possible role of topographic cross-talk (*i.e.*, coupling between measured signal and surface topography) on the ESM signal. The primary sources of cross-talk are the changes in the effective tip−surface contact area and local slope. The latter will result in the changes in direction of the forces acting on the tip (proportional to the sin of the local slope).[70] The former can both couple to the signal strength (direct topographic cross-talk, very common, *e.g.*, to SPM-based nanomechanical measurements such as atomic force acoustic microscopy)[71−73] or change contact resonant frequency leading to the spurious changes in signal for imaging frequencies close to resonant (indirect cross-talk).[74] We note that direct cross-talk is expected to be small for ESM, due to the fact that, for contact imaging, changes in contact area are relatively small and the signal is expected to scale as or slower than the first power of contact area (in fact, it is independent of contact area for a diffusionally coupled tip).[41] Second, the use of the band excitation method[56] obviates indirect topographic cross-talk. Furthermore, the BE resonant frequency image (not shown) illustrates gradual strong changes of the resonance frequency within the grains and jumps at the grain boundaries (apparently due to changes in local slope), significantly different from ESM contrast. Lastly, all forms of topographic cross-talk are generally conservative and are not expected to affect time- or voltage-dependent responses.

Principal Component Analysis of Relaxation Data. A straightforward approach for the analysis of the ESM relaxation data over the spatial grid, that is, 3D data set of $A(x,y,t)$, can be achieved using the functional fitting approach. In this, the individual spectra are fitted by an appropriately chosen function, and then the resultant fitting parameters are displayed as spatial maps. However, this approach is limited by the fact that the functional form of the relaxation law in ESM and its link to local electrochemical functionality is *a priori* unknown, and the relatively high noise level inevitable in an SPM experiment precludes phenomenological search for a fitting function. The averaging of relaxation curves over dissimilar locations, such as analysis of $A_{av}(t) = \langle A(x,y,t)\rangle_{x,y}$, cannot elucidate the single point relaxation law. As an example, averaging of multiple exponential decays with predefined (spatially dependent) relaxation time distributions can yield stretched exponent and logarithmic relaxation laws.[75]

To avoid these problems, explore the spatial variability of the relaxation behavior, and its relationship to the microstructure, and establish the veracity of fitting approach, we analyze spectroscopic ESM data using principal component analysis (PCA).[69,76,77] Previously, this approach was used for the analysis of data in the bias dependence of ESM hysteresis opening,[21] ESM spectroscopy,[22] and time domain relaxation in disordered ferroelectrics[64] and electrochemical systems.[24] In analyzing the PCA results, we note the presence of spatial correlations in the loading maps, suggesting that the corresponding component is significant and represents the intrinsic system response. PCA analysis of the relaxation data (a) suggests the presence of strongly correlated response features associated with the grain boundaries and (b) suggests that spatial variability of the relaxation behavior can be adequately described by three independent components, imposing the limits on functional fit analysis (*e.g.*, fit by a function with more than three free parameters can lead to interdependent images). Given the qualitative similarity between PCA loading maps and the fitting function analysis, the former are not shown. However, we note that the presence of these correlations is an instrumental first step in data analysis establishing veracity and spatial variability of relaxation responses from purely statistical analysis without *a priori* assumptions about the underlying response mechanisms.

Quantitative Time Domain ESM Mapping. Analysis of the time-resolved ESM data of the Si-anode device necessitates the development of mathematical models for relaxation behavior based on physical mechanisms (as opposed to phenomenological function fits, *e.g.*, exponential fit reported earlier).[24] Here, we consider two possible contrast mechanisms. In the "top electrode" model, application of the electric bias between cathode and anode generates Li-ion flux between the two. The changes in Li-ion concentration inside the anode due to ion transfer across the electrolyte−anode boundary result in inhomogeneous strains in the anode. The latter results in non-uniform strains, which are detected by the SPM tip as the vertical and lateral displacements of the top anode surface. In the "tip electrode" model, the finite conductivity of the Si

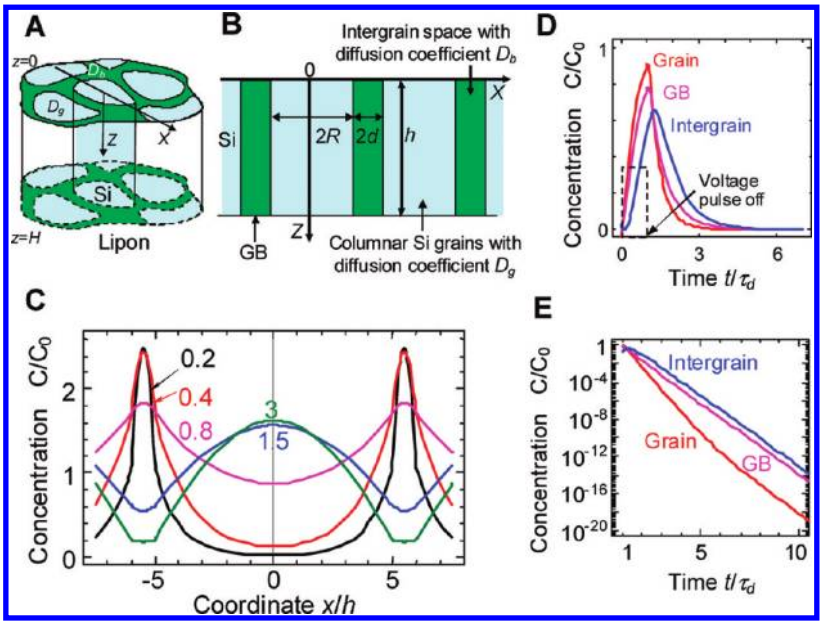

Figure 5. Si grains layout consisting of the active regions with irregular shape: "grains" (A,B) cross section of the approximate model system consisting of the identical columnar grains of width 2*R* and effective height *h*. (C) Lateral distribution of the concentration amplitude *C*(*x*) calculated (in the first approximation!) for *R*/*h* = 5, *d*/*h* = 0.5, *z* = 0, and different ratio values of the diffusion coefficients D_b/D_g (numbers near the curves). (D,E) Temporal evolution of surface concentration (*z* = 0) in linear scale (D) and its relaxation in semilogarithmic scale (E) calculated for *R*/*h* = 5, *d*/*h* = 0.5. D_b/D_g = 0.2, diffusion time $\tau_d = h^2/D_g$, and rectangular pulse duration $\tau_0 = \tau_d$.

anode results in a measurable potential drop between the (nominally grounded) anode and (grounded) conductive SPM tip. The local potential drop at the tip−surface junction results in Li-ion motion and hence local strain. We note that in both cases the slow evolution of Li-ion activity with the charge state of the device is the result of Li-ion transfer from cathode to anode, and hence evolution of the ESM image contrast with time reflects changes in the position-dependent electrochemical functionality of the device. In the following section, the possible influence of a water layer on the Si surface or water droplet around the tip due to measurements in ambient on the electric field distribution is assumed to be trivial and results solely in a change of the effective tip size.

Global ESM Mechanisms. To analyze the feasibility of highly localized ESM contrast in the top electrode case, we consider the role of lateral inhomogeneity of material on the strain distribution for the diffusion-controlled case.[41] Here, the application of the electric bias across the battery structure results in the transfer of Li ions across the electrolyte−anode interface and its subsequent (non-uniform) diffusion into the anode. In this case, the electric field within the anode is assumed to be sufficiently small due to the high carrier concentration, similar to the assumption typically employed for strain analysis in electrochemically active nanoparticles.[54,78−80] The observed ESM contrast in this case is due to the difference of the diffusivity *D* of the grain-boundary-like region (GB), D_b, and grains, D_g. For the model system shown in Figure 5A,B, we derived the analytical solution of the 2D ambipolar diffusion equation

$$\frac{\partial}{\partial t}\,\delta C(\mathbf{x}, t) = D\left(\frac{\partial^2}{\partial x_1^2}+\frac{\partial^2}{\partial x_2^2}+\frac{\partial^2}{\partial x_3^2}\right)\delta C(\mathbf{x}, t) \qquad (1)$$

describing the evolution of Li concentration $C(\mathbf{x},t)$. The effective coefficient of ambipolar diffusion, $D = (D_a\mu_c + D_c\mu_a)/(\mu_c + \mu_a)$, is independent of concentration in our approximation. $D_{a,c}$ values are the anion and cation diffusion coefficients, which we suppose are independent of concentrations, $\mu_{a,c}$ (their mobilities). Note that electrostatic potential does not contribute to the equation in the case of ambipolar diffusion.

The initial condition for eq 1 is $C(\mathbf{x},t)|_{t<0} = 0$, and the boundary conditions are $\partial C(\mathbf{x},t)/\partial z|_{z=0} = 0$ at the Li-ion-blocking/ambient interface $z = 0$ and $C(\mathbf{x},t)|_{z=h} = C_0(t) \sim V_0(t)$ at the Li-ion-conducting Si/Lipon interface $z = h$. Here, $V_0(t)$ is the time-dependent potential applied to the system that provides the driving force for Li-ion redistribution (assumed to be uniform in the anode and decreasing across the electrolyte in a usual fashion). Note that the latter condition contains the only relevant inhomogeneity of the problem, namely, the fixed concentration, $C_0(t)$, that does not contradict initial conditions.

The structure shown in Figure 5A is a typical 3D columnar structure with irregular grain shape in $\{x,y\}$ cross section and homogeneous material properties in the *z*-direction. Here, we treat the problem approximately as a 2D problem in the periodic regular 1D approximation, as shown in Figure 5B (the system is assumed to be uniform along the *y*-axis). For the simplified periodic geometry of the grain structure

shown in Figure 5B, eq 1 can be rewritten as

$$\frac{\partial}{\partial t} C(\mathbf{x}, t) = D_g \left(\frac{\partial^2}{\partial x^2} + \frac{\partial^2}{\partial z^2} \right) C(\mathbf{x}, t)$$
$$\text{at } n(R + 2d) \leq |x| \leq R + n(R + 2d) \quad \textbf{(2a)}$$

$$\frac{\partial}{\partial t} C(\mathbf{x}, t) = D_b \left(\frac{\partial^2}{\partial x^2} + \frac{\partial^2}{\partial z^2} \right) C(\mathbf{x}, t)$$
$$\text{at } n(R + 2d) + R \leq |x| < (n + 1)(R + 2d) \quad \textbf{(2b)}$$

where number $n = 0, 1, 2,...$ The parameters $2R$ and $2d$ are the grain and grain boundary region widths, respectively, h is the effective height of columnar Si grains.

Using the symmetry consideration, we seek the solution in the domain from $x = 0$ to $x = R + d$ representing "half" of the system, with the additional boundary conditions of the flux absence at grain and intergrain center planes (*i.e.*, at $x = 0$ and $x = R + d$):

$$\frac{\partial C(x, z, t)}{\partial x}\Big|_{x=0} = 0, \quad \frac{\partial C(x, z, t)}{\partial x}\Big|_{x=R+d} = 0 \quad \textbf{(3)}$$

The conditions for concentration and flux continuity are

$$C(R - 0, z, t) = C(R + 0, z, t) \quad \textbf{(4)}$$

$$D_g \frac{\partial C(x, z, t)}{\partial x}\Big|_{x=R-0} = D_b \frac{\partial C(x, z, t)}{\partial x}\Big|_{x=R+0} \quad \textbf{(5)}$$

For rectangular voltage pulse of width τ_0 and amplitude V_0, the concentration $C(\mathbf{x},t)$ at the top surface was derived in the Supporting Information and illustrated in Figure 5C–E. For times $t \gg \tau_0$, the spatial–temporal distribution of the concentration profile is determined by the series

$$C(x, z, t \gg \tau_0) \approx C_0 \sum_n f_{nm}(x) \cos\left(\frac{\pi}{h} \frac{2n - 1}{2} z \right) \exp(-\lambda_{n1}(t - \tau_0)) \quad \textbf{(6)}$$

The system relaxation is governed by the set of relaxation times

$$\lambda_{n1} \approx \left(\frac{\pi}{h} \frac{2n - 1}{2} \right)^2 \frac{dD_b + RD_g}{d + R} \quad \textbf{(7)}$$

If the convergence of series eq 6 is sufficient to cut the series at the second term, the concentration decreases with the same relaxation time in all parts of the system, while the relative concentration at the given moment of time is coordinate-dependent.

To verify the analytical model, eqs 6 and 7, and to get more insight into the temporal evolution of the concentration in the system, we performed finite element modeling (FEM) of the two-dimensional problem sketched in Figure 5B and formulated in eqs 2–5 with the following set of parameters: $h = 300$ nm, $D_g = 3 \times 10^{-12}$ m^2/s, $D_b = 0.6 \times 10^{-12}$ m^2/s (*i.e.*, $D_b/D_g = 0.2$), $2R = 3000$ nm, $2d = 300$ nm ($R/h = 5$, $d/h = 0.5$), and pulse duration $\tau_0 = 30$ ms. The simulations were performed using COMSOL v4.1 multiphysics FEM package. Figure 6a shows resulting maps of concentration distribution at different times after the application of bias pulse, and Figure 6b illustrates behavior similar to that in Figure 5D, demonstrating an excellent agreement between analytical and numerical results. Figure 6c displays average concentrations in grain and intergrain domains as functions of time to emphasize the difference in relaxation times of the domains with different diffusion coefficients. The inset illustrates that the lateral distribution of concentration along the upper surface can be transiently nonmonotonic away from the intergrain domain with sharp peaks and valleys.

Note that even a relatively small mismatch between the diffusion coefficients D_g and D_b can lead to retardation and apparent accumulation of Li in the GB if the diffusion coefficient there is lower. This behavior can be understood from the time dependence of Li concentration shown in Figures 5D,E and 6a. In the on-field stage, the Li concentration at $z = 0$ is larger in the grains, but due to the lateral flow between the grain and intergrain area, the concentrations remain comparable. In the off-field stage, Li diffuses slower from the intergrain region, resulting in a higher apparent concentration. Note that the concentration in the middle of the intergrain region is still increasing after the voltage pulse until the concentration in the grain sufficiently drops to establish a concentration gradient corresponding to outflow of the Li from the intergrain domain. The crossover between these regimes is given by lateral diffusion time $\tau_d = h^2/D_g$. Remarkably, even small differences in diffusivity between the grain boundaries and grain bulk will result in strong transient spatial localization of the Li-ion profile at the GBs.

Experimental data presented in Figure 4A suggest that the Li diffusion time has to be $\tau_d G \sim 30$ ms inside the active grain and $\tau_d^{GB} \sim 100$ ms for GB, defined as the time when 90% of the measured relaxation is complete. The corresponding diffusion coefficient becomes $D_g^G = h^2/\tau_d = 3 \times 10^{-12}$ m^2/s inside the grain and $D_g^{GB} = 0.9 \times 10^{-12}$ m^2/s at the grain boundary for the Si film thickness $h = 300$ nm used in experiments. However, the values are much higher than the value $D_g = 10^{-16}$m^2/s reported for Si by Ding *et al.*[81] Hence, we conclude that, while the global model can explain the observed Li-ion behavior assuming high Li mobility in the grains and low mobility in the grain boundaries, the required diffusion coefficients are well above those expected for this material. Therefore, we conclude that the global signal generating mechanism is not supported by the experimental data; while a qualitative picture can be reproduced, the numerical values of parameters are several orders of magnitude larger than

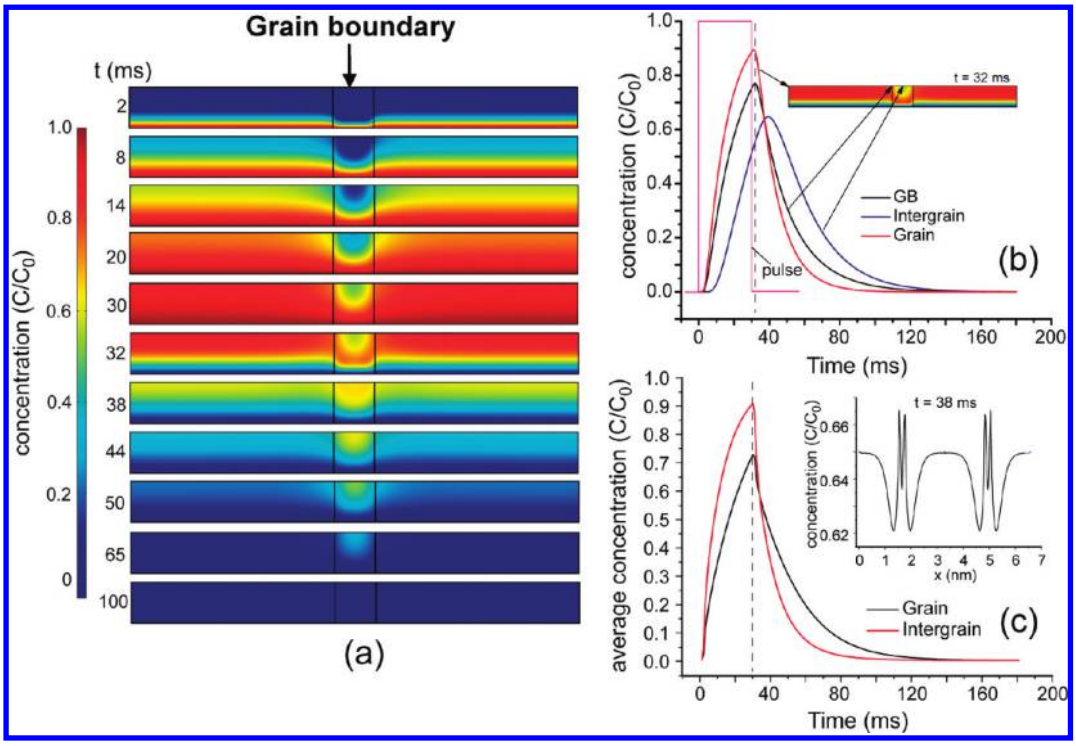

Figure 6. (a) Sequence color-coded 2D maps of the concentration distribution in the model of Figure 5B at different time moments indicated at the left edge of each map. The maps were obtained with FEM simulations for $R/h = 5$, $d/h = 0.5$ (see text for details). The left edge of the maps corresponds to $x = 0$ in Figure 5B. (b) Same as Figure 5D, but obtained with FEM simulations. (c) Average concentrations in grain and intergrain domains as functions of time. Inset shows lateral distribution of the concentration amplitude $C(x)$ for $z = 0$, similar to Figure 5C, for the case $D_b/D_g = 0.2$ at a time $t = 38$ ms, *i.e.*, close to the crossover point.

expected. Furthermore, such high Li mobility would imply very rapid charge–discharge rates for the device that are not experimentally observed.[22]

We further note that additional contribution to observed Li-ion dynamics in the global case can be the migration transport due to the non-uniform electric field at microstructural elements such as GBs. In this case, the electric fields within the anode are highly inhomogeneous and non-negligible due to the limited conductivity of the Si, inducing the ionic flow in the field on-state and leading to preferential increase of Li concentration in grain boundary regions. In the off-state, the relaxation is controlled by ambipolar diffusion. In this case, the general estimate of the diffusion times can still be obtained from observed relaxation curves. However, the upper boundary of diffusion length is estimated as an observed grain boundary width in the ESM image of the order of ~10 nm, leading to diffusion coefficients on the order of the value $D_g = 10^{-15}$ m^2/s, close to bulk values. However, such lateral motion of Li in the material would be expected to lead to significant changes of the contrast outside of the GB region, which is not observed in the present case.

Local ESM Mechanisms. An alternative explanation for the observed phenomena is the ESM response induced by the non-uniform electric field at the tip–surface junction. This is possible if the electric field in the anode is non-negligible due to the finite conductivity of the Si, inducing a potential drop in the tip–surface junction and hence ionic flow. While the description of the ESM signal for the case of diffusion–migration transport is not yet available, some insight into this behavior can be obtained from the pure diffusion case considered previously.[55] Similarly to the global case, evolution of the Li-ion concentration field is described by the ambipolar diffusion, eq 1, where D is now (concentration-independent) local diffusion coefficient. The localization of the field on the tip–surface junction allows one to define trivial boundary conditions as $\delta C(x_1,x_2,x_3 \rightarrow \infty,t) \rightarrow 0$ and $\delta C(\mathbf{x},0) = 0$. The strain response of material was derived[55] for the general third kind boundary conditions:[82]

$$\lambda \frac{\partial}{\partial x_3} \delta C(x_1, x_2, 0, t) - \eta \delta C(x_1, x_2, 0, t) = -V_0(x_1, x_2, t) \quad (8)$$

This defines the relationship between applied bias and concentration/flux at the tip–surface junction. Here $V_0(x_1,x_2,t)$ is the electrostatic potential distribution at the tip electrode $x_3 = 0$. This boundary condition reduces to the case of either fixed concentration or fixed ionic flux at phenomenological exchange coefficient $\lambda = 0$ or $\eta = 0$, correspondingly.

The solutions were derived for the time response of the tip following the application of a rectangular

voltage pulse, $V_0(t) = V_a(\theta(t) - \theta(t - t_0))$, with pulse duration t_0 ($\theta(t)$ is the Heaviside step function). For the fixed concentration scenario, $\lambda = 0$, in which the voltage pulse is equivalent to the concentration pulse at the junction, the response was obtained as

$$u_3(0, t < t_0) \approx -(1+\nu)\frac{4\beta V_a}{\eta\sqrt{\pi}}\sqrt{Dt} \quad (9a)$$

$$u_3(0, t \gg t_0) \approx -(1+\nu)\frac{\beta V_a R_0^2 t_0}{6\eta\sqrt{\pi}Dt^{3/2}} \quad (9b)$$

The response amplitude increases with t_0 as $u_3(0,t_0) \sim (t_0)^{1/2}$ and decay when the pulse is off according to the power law $u_3(0,t \gg t_0) \sim t^{-3/2}$. Here R_0 is tip−surface contact radius, β is Vegard expansion coefficient, and ν is Poisson ratio of the material.

For the fixed flux scenario, $\eta = 0$, in which bias pulse is equivalent to the fixed ionic flux at the junction, the response increase with the bias pulse duration is logarithmic

$$u_3(0, t) \approx -(1+\nu)\beta V_a\frac{R_0^2}{4\lambda}\ln\left(1+\frac{8Dt}{R_0^2}\right) \quad (10a)$$

at $t < t_0$, while the response decay when the bias pulse is turned off is quasi-logarithmic

$$u_3(0, t) \approx -(1+\nu)\beta V_a\frac{R_0^2}{4\lambda}\ln\left(\frac{R_0^2+8Dt}{R_0^2+8D(t-t_0)}\right) \quad (10b)$$

at $t > t_0$, and then tends to the power law $u_3(0,t \gg t_0) \sim t^{-1}$.

We note that the dynamics described by eqs 10a and 10b is very close to that obtained in Figure 3C, in which response is linear in pulse magnitude and logarithmic in time. To describe the experimentally measured relaxation data, eq 10b is rewritten as

$$A \approx A_0 + B\ln\left(\frac{\tau_a + t_0 + t_1}{\tau_a + t_1}\right) \quad (11)$$

where t_1 is the time elapsed from the end of the pulse, t_0 is pulse length (defined by experimental conditions) and $\tau_a = {R_0}^2/8D$.

Using the formalism developed above for the local ESM contrast, we analyze the relaxation kinetics after the first negative pulse ($i = 1$). The time dynamics of the response in each spatial point is fitted by the logarithmic relaxation of the form $A(t) = A_0 + \Delta A\ln\lfloor(t + \tau + t_p)/(t + \tau)\rfloor$, where $A(t)$ is the measured ESM signal, A_0 is offset, ΔA is relaxation amplitude, and τ is relaxation time.

We note that this choice of the fitting function both follows from the analytical model and also allows reliable separation of response into dynamic (relaxation amplitude) and static (offset) components. The use of phenomenological relaxation functions (stretched exponent) can improve the fit, but the number of independent parameters in this case exceeds the number of significant PCA components. The use of power law leads to very low powers, indicative of the poor applicability of the model. Finally, logarithmic fit offers reasonable fit quality. However, the relaxation curves generally cannot be linearized in log coordinates.

Shown in Figure 7 are the spatially resolved maps of the $A_0(x,y)$, $\Delta A(x,y)$, and $\tau(x,y)$, providing insight into spatial variability of the relaxation behavior. The amplitude and offset of the relaxation curves exhibit strong variability across the surface, with clear maxima at the grain-boundary-like features (Figure 7A,B) as expected. Within the grain-like areas, the relaxation time is close to zero due to the small ESM signals there, and in the boundary-like regions, a relaxation time of approximately 4 ms can be extracted. Using $\tau_a = {R_0}^2/8D$ and the extracted diffusion time with an estimated tip radius of 10 nm, the Li diffusivity can be estimated to $D_l^{GB} = 3 \times 10^{-15}$ m^2/s, which is much closer to values reported in the literature. Therefore, we conclude that the local ESM analysis is more appropriate for the investigated sample system compared to the global analysis which resulted in much higher diffusivity values.

Evolution of Li Dynamics with Charge State and Conductance Imaging. The bipolar pulse sequence described above was used in order to establish reproducibility and minimize the irreversible changes in the battery. However, as discussed in the previous section, irreversible changes in the ESM signal are observed as different offsets of the ESM signal after relaxation for positive and negative voltage pulses. It was observed that the ESM response after voltage pulses evolved with increasing number of pulses applied to the battery, similar to earlier studies.[21,22] This behavior was also observed in single point measurements with unipolar pulses, as shown in the increasing offset in Figure 2. The reason why the ESM relaxation behavior changes as a function of cycle numbers can be explained by a partial charging of the battery through our measurement procedure; that is, the concentration of Li ions is increased in the Si anode, which gives rise to a higher ESM signal.

The results in Figures 2, 3, and 7 were obtained on a sample whose relaxation signal was well developed after approximately 2×10^5 bipolar measurement cycles applied to the battery (with an approximate frequency of 0.5 Hz) . Figure 8A−C shows the fitted relaxation parameter offset, relaxation amplitude, and relaxation time from the same area as in Figure 7 after a lower number of measurement cycles (2×10^4). The scale bars are chosen to be the same as in Figure 7 for easier comparison of the two data sets. It is clearly visible that the ESM relaxation is mostly uniform across the whole area and that most of the boundary-like features do not show an enhanced ESM signal after the applied voltage pulse. Figure 8D−F displays the

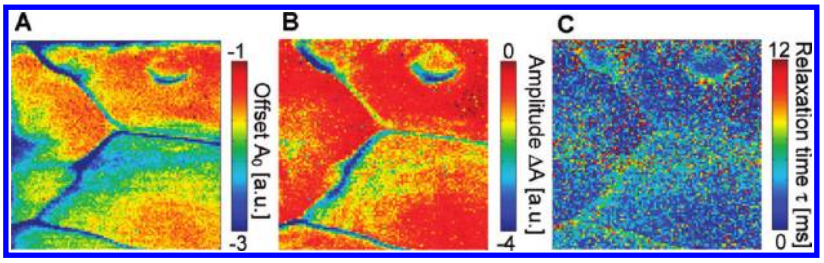

Figure 7. (A) Map of fitted signal offset, (B) relaxation amplitude, and (C) relaxation time for the 1 × 1 μm^2 region on the amorphous Si surface shown in Figure 4B after the first negative pulse (i = 1).

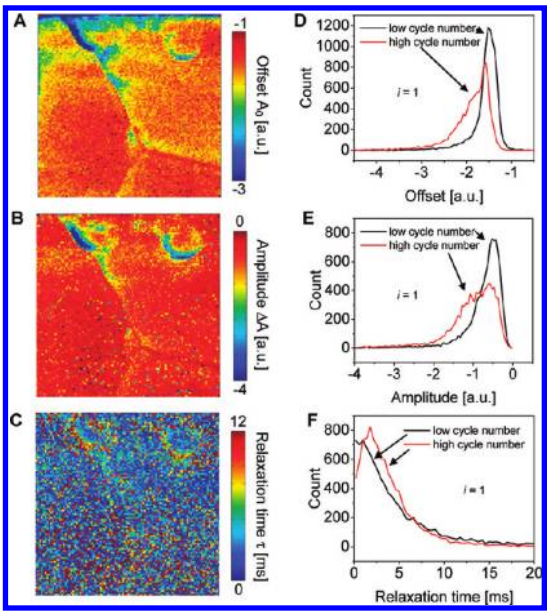

Figure 8. Spatial distribution of fitted (A) offset, (B) relaxation amplitude, and (C) relaxation time for the region on the amorphous Si surface shown in Figure 4B after the first negative pulse (i = 1). Histograms of (D) offset, (E) relaxation amplitude, and (F) relaxation time for pristine and aged sample.

histograms from the relaxation map of a sample exposed to low cycle numbers and high cycle numbers for comparison. Note that the cycled sample has significantly higher (in absolute value) relaxation amplitude and offset, illustrating the progressive increase in electromechanical activity with Li-ion intercalation in the anode material. Furthermore, for low cycle number (uncharged) material, the relaxation time contribution is centered at zero (and hence the averaged behavior is dominated by the statistical errors), while for high cycle numbers, a statistically significant peak is observed.

The high localization of the increased relaxation amplitude at the boundary-like features and their evolution during the charging process can be explained by several scenarios, including (a) preferential Li-ion localization at the boundaries, (b) different diffusion coefficients/mobilities, (c) difference in conductivity and hence preferential field concentration, or (d) difference in mechanical properties. We note that the difference in mechanical properties is expected to be a

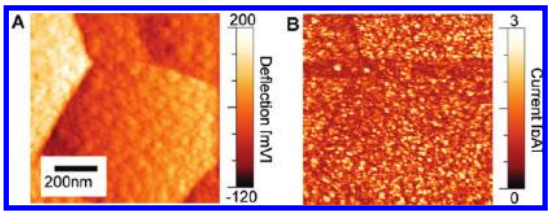

Figure 9. Deflection and cAFM image measured at 0.5 V_{dc} in a 1 × 1 μm area on the a-Si anode of a comparable thin-film battery structure (different sample from the same series).

minor effect in the ESM contrast since relative motion of the grains would produce a different response pattern (rapid variation at the interfaces as opposed to the maxima at the interfaces). While the Li-ion concentration (a) cannot be accessed independently by ESM, we note that the full length of the measurements (several days) is large enough for the concentration gradients to equilibrate within the material. Hence, we attribute the enhanced ESM signal at the GBs to the higher mobility of the Li ions, which can be ascribed both to higher diffusion coefficients and low conductivity of the GB region that results in preferential Li accumulation under the field effect.

Finally, to differentiate the latter two possibilities, shown in Figure 9 is the conductive AFM (cAFM) image of the Si anode from the same device series. Note, the graininess of the image and the presence of a number of conductive spots (possibly associated with surface roughness). However, no low-conductivity features associated with the grain boundaries can be identified at these imaging conditions. Correspondingly, we attribute the observed ESM contrast to differences in ionic mobilities/diffusivities within the grain boundary regions.

We further note that the observed concentration of the electrochemical strains at the GB region as directly observed by ESM can be an origin of the Si-anode degradation that severely limits the broad use of this material. The conductive channels along the GBs can act as shunts connecting the electrolyte and current collector and precluding the bulk of the Si grain from participating in charge–discharge process, thus contributing to the irreversible capacity losses. Overall, ESM can be an ideal tool for exploring the role of microstructure, patterning, or surface on the functionality of these materials.

SUMMARY

To summarize, we demonstrate an approach for direct quantitative measurements and spatially resolved mapping of diffusion times in nanometer scale volumes, exceeding the detection limits of classical electrochemical methods by 6−8 orders of magnitude. We directly map the Li-ion dynamics in amorphous Si anode and demonstrate its concentration in a small number of well-localized regions associated with the grain-boundary-like features. The comparison of observed relaxation kinetics, dependence of response on bias pulse parameters, and spatial resolution suggests that the ESM signal originates at the tip−surface junction. The localization of ESM signal at interfaces indicates that the latter are responsible for mechanical stability and irreversible capacity loss in Si anodes, suggesting possible strategies for optimization of these materials.

We further note that high ionic diffusion coefficients and strong coupling between the molar volume and ionic concentration are universal for all energy storage and conversion materials, as well as mixed ionic−electronic conductors used in electroresistive and memristive systems. The ESM approach can be expected to be universally applicable to these materials systems, providing yet unavailable details of ionic transport on the nanoscale.

MATERIALS AND METHODS

The rechargeable thin-film batteries obtained here consisted of Si/LiPON/$LiCoO_2$ structures on Au/Ni-coated Al_2O_3 substrates. Before depositing the $LiCoO_2$ cathode films, an Al stencil mask was used to cover the Au/Ni-coated Al_2O_3 substrates and define the cathode areas with 0.2 cm diameter. The ~0.5 μm thick $LiCoO_2$ cathode films were fabricated on the substrates using a RF-magnetron sputtering technique at 50 W deposition power (159 V). The films were annealed at 800 °C for 2 h in an O_2 flowing quartz tube furnace. The amorphous LiPON electrolytes (~1 μm thick) were deposited on the $LiCoO_2$ films using the same sputtering technique with 70 W (230 V). Finally, amorphous Si anodes of ~350 nm thickness were deposited on the LiPON film electrolytes using a DC-magnetron sputtering technique.

Atomic force microscopy (AFM) measurements were performed on a commercial system (Nanoman V, Bruker, Santa Barbara, CA) equipped with LabView/Matlab-based band excitation controller implemented on a PXI-5122/PXI-5412 fast DAQ card in ambient atmosphere without any additional humidity control. ESM was performed with 200−400 kHz 2 V_{ac} band excitation signal applied to the bottom electrode of the battery device. This bias amplitude is chosen well within the linearity regime of the response. The AFM tip (PPP-EFM Nanosensors, Pt/Ir coating) and the top electrode were grounded to minimize electrostatic signal contribution and electrochemical processes at the tip−surface junction. ESM time spectroscopy was performed by applying a well-defined voltage pulse and measuring the ESM signal afterward as a function of time for typically 250−500 ms. Conductive AFM images were obtained by applying 0.5 V_{dc} to the AFM tip during scanning and measuring the current simultaneously.

Acknowledgment. This work is supported in part by the Fluid Interface Reactions, Structures and Transport (FIRST) Center, an Energy Frontier Research Center funded by the U.S. DOE BES. SPM imaging was conducted at the Center for Nanophase Materials Sciences, which is sponsored at Oak Ridge National Laboratory by the Office of Basic Energy Sciences, U.S. Department of Energy.

Supporting Information Available: Derivation of the time- and position-dependent ionic concentration t the Si-anode surface after application of rectangular voltage pulse of width τ_0 and amplitude V_0 to the SPM tip. This material is available free of charge *via* the Internet at http://pubs.acs.org.

REFERENCES AND NOTES

1. Nazri, G. A.; Pistoia, G. *Lithium Batteries: Science and Technology*; Springer Verlag: Berlin, 2009.
2. Bagotsky, V. S. *Fuel Cells: Problems and Solutions*; Wiley: New York, 2009.
3. O'Hayre, R.; Cha, S. W.; Colella, W.; Prinz, F. B. *Fuel Cell Fundamentals*; Wiley: New York, 2006.
4. Sawa, A. Resistive Switching in Transition Metal Oxides. *Mater. Today* **2008**, *11*, 28–36.
5. Strukov, D. B.; Snider, G. S.; Stewart, D. R.; Williams, R. S. The Missing Memristor Found. *Nature* **2008**, *453*, 80–83.
6. Garcia-Barriocanal, J.; Rivera-Calzada, A.; Varela, M.; Sefrioui, Z.; Iborra, E.; Leon, C.; Pennycook, S. J.; Santamaria, J. Colossal Ionic Conductivity at Interfaces of Epitaxial ZrO_2:Y_2O_3/$SrTiO_3$ Heterostructures. *Science* **2008**, *321*, 676–680.
7. Kern, K.; Maier, J. Nanoionics and Nanoelectronics. *Adv. Mater.* **2009**, *21*, 2569–2569.
8. Adler, S.; Russek, S.; Reimer, J.; Fendorf, M.; Stacy, A.; Huang, Q. Z.; Santoro, A.; Lynn, J.; Baltisberger, J.; Werner, U. Local-Structure and Oxide-Ion Motion in Defective Perovskites. *Solid State Ionics* **1994**, *68*, 193–211.
9. Li, J.; Dahn, J. R. An *In Situ* X-ray Diffraction Study of the Reaction of Li with Crystalline Si. *J. Electrochem. Soc.* **2007**, *154*, A156–A161.
10. Obrovac, M. N.; Krause, L. J. Reversible Cycling of Crystalline Silicon Powder. *J. Electrochem. Soc.* **2007**, *154*, A103–A108.
11. Li, J.; Smith, A.; Sanderson, R. J.; Hatchard, T. D.; Dunlap, R. A.; Dahn, J. R. *In Situ* (119)Sn Mossbauer Effect Study of the Reaction of Lithium with Si Using a Sn Probe. *J. Electrochem. Soc.* **2009**, *156*, A283–A288.
12. Hatchard, T. D.; Dahn, J. R. *In Situ* XRD and Electrochemical Study of the Reaction of Lithium with Amorphous Silicon. *J. Electrochem. Soc.* **2004**, *151*, A838–A842.
13. Chevrier, V. L.; Dahn, J. R. First Principles Model of Amorphous Silicon Lithiation. *J. Electrochem. Soc.* **2009**, *156*, A454–A458.
14. Chevrier, V. L.; Dahn, J. R. First Principles Studies of Disordered Lithiated Silicon. *J. Electrochem. Soc.* **2010**, *157*, A392–A398.
15. Lewis, R. B.; Timmons, A.; Mar, R. E.; Dahn, J. R. *In Situ* AFM Measurements of the Expansion and Contraction of Amorphous Sn-Co-C Films Reacting with Lithium. *J. Electrochem. Soc.* **2007**, *154*, A213–A216.
16. Obrovac, M. N.; Christensen, L.; Le, D. B.; Dahn, J. R. Alloy Design for Lithium-Ion Battery Anodes. *J. Electrochem. Soc.* **2007**, *154*, A849–A855.
17. Chan, C. K.; Peng, H. L.; Liu, G.; Mcllwrath, K.; Zhang, X. F.; Huggins, R. A.; Cui, Y. High-Performance Lithium Battery Anodes Using Silicon Nanowires. *Nat. Nanotechnol* **2008**, *3*, 31–35.
18. Magasinski, A.; Dixon, P.; Hertzberg, B.; Kvit, A.; Ayal, J.; Yushin, G. High-Performance Lithium-Ion Anodes Using a Hierarchical Bottom-Up Approach. *Nat. Mater.* **2010**, *9*, 353–358.
19. Li, J.; Christensen, L.; Obrovac, M. N.; Hewitt, K. C.; Dahn, J. R. Effect of Heat Treatment on Si Electrodes Using Polyvinylidene Fluoride Binder. *J. Electrochem. Soc.* **2008**, *155*, A234–A238.

20. Weppner, W.; Huggins, R. A. Electrochemical Methods for Determining Kinetic-Properties of Solids. *Annu. Rev. Mater. Sci.* **1978**, *8*, 269–311.
21. Balke, N.; Jesse, S.; Kim, Y.; Adamczyk, L.; Ivanov, I. N.; Dudney, N. J.; Kalinin, S. V. Decoupling Electrochemical Reaction and Diffusion Processes in Ionically-Conductive Solids on the Nanometer Scale. *ACS Nano* **2010**, *4*, 7349–7357.
22. Balke, N.; Jesse, S.; Kim, Y.; Adamczyk, L.; Tselev, A.; Ivanov, I. N.; Dudney, N. J.; Kalinin, S. V. Real Space Mapping of Li-Ion Transport in Amorphous Si Anodes with Nanometer Resolution. *Nano Lett.* **2010**, *10*, 3420–3425.
23. Balke, N.; Jesse, S.; Morozovska, A. N.; Eliseev, E.; Chung, D. W.; Kim, Y.; Adamczyk, L.; Garcia, R. E.; Dudney, N.; Kalinin, S. V. Nanoscale Mapping of Ion Diffusion in a Lithium-Ion Battery Cathode. *Nat. Nanotechnol.* **2010**, *5*, 749–754.
24. Guo, S.; Jesse, S.; Kalnaus, S.; Balke, N.; Daniel, C.; Kalinin, S. V. Direct Mapping of Ion Diffusion Times on $LiCoO_2$ Surfaces with Nanometer Resolution. *J. Electrochem. Soc.* **2011**, *158*, A982–A990.
25. Fleig, J.; Baumann, F. S.; Brichzin, V.; Kim, H. R.; Jamnik, J.; Cristiani, G.; Habermeier, H. U.; Maier, J. Thin Film Microelectrodes in SOFC Electrode Research. *Fuel Cells* **2006**, *6*, 284–292.
26. La O, G. J.; In, H. J.; Crumlin, E.; Barbastathis, G.; Shao-Horn, Y. Recent Advances in Microdevices for Electrochemical Energy Conversion and Storage. *Int. J. Energy Res.* **2007**, *31*, 548–575.
27. Opitz, A. K.; Fleig, J. Investigation of O_2 Reduction on Pt/YSZ by Means of Thin Film Microelectrodes: The Geometry Dependence of the Electrode Impedance. *Solid State Ionics* **2010**, *181*, 684–693.
28. Bard, A. J.; Faulkner, L. R. *Electrochemical Methods: Fundamentals and Applications*; John Wiley & Sons: New York, 2001.
29. Ho, C.; Raistrick, I. D.; Huggins, R. A. Application of AC Techniques to the Study of Lithium Diffusion in Tungsten Trioxide Thin-Films. *J. Electrochem. Soc.* **1980**, *127*, 343–350.
30. Newman, J. S.; Thomas-Alyea, K. E. *Electrochemical Systems*; Wiley-Interscience: New York, 2004.
31. Weppner, W.; Huggins, R. A. Determination of Kinetic-Parameters of Mixed-Conducting Electrodes and Application to System Li_3Sb. *J. Electrochem. Soc.* **1977**, *124*, 1569–1578.
32. Orazem, M. E.; Tribollet, B. *Electrochemical Impedance Spectroscopy*; Wiley: New York, 1902.
33. Gruverman, A.; Auciello, O.; Tokumoto, H. Imaging and Control of Domain Structures in Ferroelectric Thin Films *via* Scanning Force Microscopy. *Annu. Rev. Mater. Sci.* **1998**, *28*, 101–123.
34. Gruverman, A.; Kholkin, A. Nanoscale Ferroelectrics: Processing, Characterization and Future Trends. *Rep. Prog. Phys.* **2006**, *69*, 2443–2474.
35. Morozovska, A. N.; Eliseev, E. A.; Kalinin, S. V. Electromechanical Probing of Ionic Currents in Energy Storage Materials. *Appl. Phys. Lett.* **2010**, *96*, 222906.
36. Amatucci, G. G.; Tarascon, J. M.; Klein, L. C. CoO_2, the End Member of the Li_xCoO_2 Solid Solution. *J. Electrochem. Soc.* **1996**, *143*, 1114–1123.
37. Butt, H. J.; Cappella, B.; Kappl, M. Force Measurements with the Atomic Force Microscope: Technique, Interpretation and Applications. *Surf. Sci. Rep.* **2005**, *59*, 1–152.
38. García, R. *Amplitude Modulation Atomic Force Microscopy*; Wiley-VCH: Weinheim, Germany, 2010.
39. Garcia, R.; Perez, R. Dynamic Atomic Force Microscopy Methods. *Surf. Sci. Rep.* **2002**, *47*, 197–301.
40. Sarid, D. *Scanning Force Microscopy*; Oxford University Press: New York, 1994.
41. Morozovska, A. N.; Eliseev, E. A.; Balke, N.; Kalinin, S. V. Local Probing of Ionic Diffusion by Electrochemical Strain Microscopy: Spatial Resolution and Signal Formation Mechanisms. *J. Appl. Phys.* **2010**, *108*, 053712.
42. Morozovska, A. N.; Eliseev, E. A.; Tagantsev, A. K.; Bravina, S. L.; Chen, L. Q.; Kalinin, S. V. Thermodynamics of Electromechanically Coupled Mixed Ionic-Electronic Conductors: Deformation Potential, Vegard Strains, and Flexoelectric Effect. *Phys. Rev. B* **2011**, *83*, 195313.
43. Dudney, N. J. Solid-State Thin-Film Rechargeable Batteries. *Mater. Sci. Eng. B* **2005**, *116*, 245–249.
44. Chen, L. B.; Xie, J. Y.; Yu, H. C.; Wang, T. H. An Amorphous Si Thin Film Anode with High Capacity and Long Cycling Life for Lithium Ion Batteries. *J. Appl. Electrochem.* **2009**, *39*, 1157–1162.
45. Das, S. R.; Williams, D. F.; Webb, J. B. Dependence of the Microstructure of Amorphous-Silicon Thin-Films Prepared by Planar RF Magnetron Sputtering on Deposition Parameters. *J. Appl. Phys.* **1983**, *54*, 3101–3105.
46. Messier, R.; Giri, A. P.; Roy, R. A. Revised Structure Zone Model for Thin-Film Physical Structure. *J. Vac. Sci. Technol., A* **1984**, *2*, 500–503.
47. Messier, R.; Ross, R. C. Evolution of Microstructure in Amorphous Hydrogenated Silicon. *J. Appl. Phys.* **1982**, *53*, 6220–6225.
48. Stievenard, D.; Legrand, B. Silicon Surface Nano-Oxidation Using Scanning Probe Microscopy. *Prog. Surf. Sci.* **2006**, *81*, 112–140.
49. Scovell, D. L.; Pinkerton, T. D.; Finlayson, B. A.; Stuve, E. M. The Dielectric Response of Water in High Electric Fields: Equilibrium Water Thickness and the Field Distribution. *Chem. Phys. Lett.* **1998**, *294*, 255–261.
50. Weeks, B. L.; Vaughn, M. W.; DeYoreo, J. J. Direct Imaging of Meniscus Formation in Atomic Force Microscopy Using Environmental Scanning Electron Microscopy. *Langmuir* **2005**, *21*, 8096–8098.
51. Bussian, D. A.; O'Dea, J. R.; Metiu, H.; Buratto, S. K. Nanoscale Current Imaging of the Conducting Channels in Proton Exchange Membrane Fuel Cells. *Nano Lett.* **2007**, *7*, 227–232.
52. Kostecki, R.; Kong, F. P.; Matsuo, Y.; McLarnon, F. Interfacial Studies of a Thin-Film $Li_2Mn_4O_9$ Electrode. *Electrochim. Acta* **1999**, *45*, 225–233.
53. Kostecki, R.; McLarnon, F. Local-Probe Studies of Degradation of Composite $LiNi_{0.8}Co_{0.15}Al_{0.05}O_2$ Cathodes in High-Power Lithium-Ion Cells. *Electrochem. Solid State Lett* **2004**, *7*, A380–A383.
54. McEvoy, T. M.; Stevenson, K. J. Spatially Resolved Imaging of Inhomogeneous Charge Transfer Behavior in Polymorphous Molybdenum Oxide. I. Correlation of Localized Structural, Electronic, and Chemical Properties Using Conductive Probe Atomic Force Microscopy and Raman Microprobe Spectroscopy. *Langmuir* **2005**, *21*, 3521–3528.
55. Harnagea, C.; Alexe, M.; Hesse, D.; Pignolet, A. Contact Resonances in Voltage-Modulated Force Microscopy. *Appl. Phys. Lett.* **2003**, *83*, 338–340.
56. Jesse, S.; Kalinin, S. V.; Proksch, R.; Baddorf, A. P.; Rodriguez, B. J. The Band Excitation Method in Scanning Probe Microscopy for Rapid Mapping of Energy Dissipation on the Nanoscale. *Nanotechnology* **2007**, *18*, 435503.
57. Kos, A. B.; Hurley, D. C. Nanomechanical Mapping with Resonance Tracking Scanned Probe Microscope. *Meas. Sci. Technol.* **2008**, *19*, 015504.
58. Nath, R.; Chu, Y. H.; Polomoff, N. A.; Ramesh, R.; Huey, B. D. High Speed Piezoresponse Force Microscopy: <1 Frame Per Second Nanoscale Imaging. *Appl. Phys. Lett.* **2008**, *93*, 072905.
59. Rodriguez, B. J.; Callahan, C.; Kalinin, S. V.; Proksch, R. Dual-Frequency Resonance-Tracking Atomic Force Microscopy. *Nanotechnology* **2007**, *18*, 475504.
60. Guo, S.; Ovchinnikov, O. S.; Curtis, M. E.; Johnson, M. B.; Jesse, S.; Kalinin, S. V. Spatially Resolved Probing of Preisach Density in Polycrystalline Ferroelectric Thin Films. *J. Appl. Phys.* **2010**, *108*, 084103.
61. Jesse, S.; Maksymovych, P.; Kalinin, S. V. Rapid Multidimensional Data Acquisition in Scanning Probe Microscopy Applied to Local Polarization Dynamics and Voltage Dependent Contact Mechanics. *Appl. Phys. Lett.* **2008**, *93*, 112903.

62. Kalinin, S. V.; Rodriguez, B. J.; Jesse, S.; Morozovska, A. N.; Bokov, A. A.; Ye, Z. G. Spatial Distribution of Relaxation Behavior on the Surface of a Ferroelectric Relaxor in the Ergodic Phase. *Appl. Phys. Lett.* **2009**, *95*, 142902.
63. Kholkin, A. L.; Shvartsman, V. V.; Kiselev, D. A. Nanoscale Characterization of Ferroelectric Materials for Piezoelectric Applications. *Ferroelectrics* **2006**, *341*, 3–19.
64. Rodriguez, B. J.; Jesse, S.; Morozovska, A. N.; Svechnikov, S. V.; Kiselev, D. A.; Kholkin, A. L.; Bokov, A. A.; Ye, Z. G.; Kalinin, S. V. Real Space Mapping of Polarization Dynamics and Hysteresis Loop Formation in Relaxor-Ferroelectric $PbMg_{1/3}Nb_{2/3}O_3$-$PbTiO_3$ Solid Solutions. *J. Appl. Phys.* **2010**, *108*, 042006.
65. Shvartsman, V.; Tyunina, A.; Levoska, J.; Kholkin, A. Local Electromechanical Properties of $PbMg_{1/3}Nb_{2/3}O_3$ Thin Films Studied by Piezoelectric Force Microscopy. *Ferroelectrics* **2004**, *302*, 569–572.
66. Shvartsman, V. V.; Kholkin, A. L.; Tyunina, M.; Levoska, J. Relaxation of Induced Polar State in Relaxor $PbMg_{1/3}Nb_{2/3}O_3$ Thin Films Studied by Piezoresponse Force Microscopy. *Appl. Phys. Lett.* **2005**, *86*, 222907.
67. Kholkin, A. L.; Bdikin, I. K.; Kiselev, D. A.; Shvartsman, V. V.; Kim, S. H. Nanoscale Characterization of Polycrystalline Ferroelectric Materials for Piezoelectric Applications. *J. Electroceram.* **2007**, *19*, 83–96.
68. Kalinin, S. V.; Rodriguez, B. J.; Budai, J. D.; Jesse, S.; Morozovska, A. N.; Bokov, A. A.; Ye, Z. G. Direct Evidence of Mesoscopic Dynamic Heterogeneities at the Surfaces of Ergodic Ferroelectric Relaxors. *Phys. Rev. B* **2010**, *81*, 064107.
69. Jesse, S.; Kalinin, S. V. Principal Component and Spatial Correlation Analysis of Spectroscopic-Imaging Data in Scanning Probe Microscopy. *Nanotechnology* **2009**, *20*, 085714.
70. Hutter, J. L. Comment on Tilt of Atomic Force Microscope Cantilevers: Effect on Spring Constant and Adhesion Measurements. *Langmuir* **2005**, *21*, 2630–2632.
71. Burnham, N. A.; Kulik, A. J.; Gremaud, G.; Gallo, P. J.; Oulevey, F. Scanning Local-Acceleration Microscopy. *J. Vac. Sci. Technol., B* **1996**, *14*, 794–799.
72. Rabe, U.; Scherer, V.; Hirsekorn, S.; Arnold, W. Nanomechanical Surface Characterization by Atomic Force Acoustic Microscopy. *J. Vac. Sci. Technol., B* **1997**, *15*, 1506–1511.
73. Yamanaka, K.; Ogiso, H.; Kolosov, O. Ultrasonic Force Microscopy for Nanometer Resolution Subsurface Imaging. *Appl. Phys. Lett.* **1994**, *64*, 178–180.
74. Jesse, S.; Guo, S.; Kumar, A.; Rodriguez, B. J.; Proksch, R.; Kalinin, S. V. Resolution Theory, and Static and Frequency-Dependent Cross-Talk in Piezoresponse Force Microscopy. *Nanotechnology* **2010**, *21*, 405703.
75. Jonscher, A. K. *Dielectric Relaxation in Solids*; Chelsea Dielectric Press Ltd.: London, 1983.
76. Bonnet, N. Some Trends in Microscope Image Processing. *Micron* **2004**, *35*, 635–653.
77. Bosman, M.; Watanabe, M.; Alexander, D. T. L.; Keast, V. J. Mapping Chemical and Bonding Information Using Multivariate Analysis of Electron Energy-Loss Spectrum Images. *Ultramicroscopy* **2006**, *106*, 1024–1032.
78. Cheng, Y. T.; Verbrugge, M. W. The Influence of Surface Mechanics on Diffusion Induced Stresses within Spherical Nanoparticles. *J. Appl. Phys.* **2008**, *104*, 083521.
79. Zhang, X. C.; Sastry, A. M.; Shyy, W. Intercalation-Induced Stress and Heat Generation within Single Lithium-Ion Battery Cathode Particles. *J. Electrochem. Soc.* **2008**, *155*, A542–A552.
80. Zhang, X. C.; Shyy, W.; Sastry, A. M. Numerical Simulation of Intercalation-Induced Stress in Li-Ion Battery Electrode Particles. *J. Electrochem. Soc.* **2007**, *154*, A910–A916.
81. Ding, N.; Xu, J.; Yao, Y. X.; Wegner, G.; Fang, X.; Chen, C. H.; Lieberwirth, I. Determination of the Diffusion Coefficient of Lithium Ions in Nano-Si. *Solid State Ion* **2009**, *180*, 222–225.
82. Carslaw, H. S.; Jaeger, J. C. *Conduction of Heat in Solids*; Clarendon: Oxford, 1959.